# Absorption and Luminescence Spectroscopy of $MnO_4^{2-}$-Doped Crystals of $BaSO_4$

**Thomas C. Brunold and Hans U. Güdel***

Departement für Chemie, Freiestrasse 3, Universität Bern, CH-3000 Bern 9, Switzerland

*Received September 26, 1996*[⊗]

The first polarized low-temperature absorption and luminescence spectra of manganese-doped crystals of $BaSO_4$ containing essentially $MnO_4^{2-}$ are reported. By using a flux composed of NaCl, KCl, and CsCl we were able to grow $BaSO_4$:$Mn^{6+}$ crystals below 620 °C. This prevents the simultaneous presence of $MnO_4^{3-}$ besides $MnO_4^{2-}$, which was mainly responsible for the erroneous assignments of the absorption spectrum in the literature. In the $BaSO_4$ host the $MnO_4^{2-}$ ion occupies a site of $C_s$ symmetry, and the orbital degeneracies of the E and T states are thus lifted. Above 16 000 $cm^{-1}$ the absorption spectra consist of a series of intense ligand-to-metal charge transfer (LMCT) excitations. Their marked polarization dependence allows an unambiguous band assignment in the parent $T_d$ symmetry. The three origins of the $^2E \rightarrow {}^2T_2$ ligand-field (LF) transition peak at 11 074, 11 570, and 11 790 $cm^{-1}$. The lowest-energy component of $^2T_2$ serves as the initial state for broadband luminescence in the near-infrared (near-IR) region with a maximum at 9300 $cm^{-1}$. Below 100 K the quantum yield is unity and the radiative lifetime is 2.75 $\mu$s, and at 300 K the quantum yield is still 20%. In both the $^2E \leftrightarrow {}^2T_2$ (d → d) absorption and luminescence spectra the vibrational structure is dominated by progressions in O−Mn−O bending modes whereas coupling to the totally symmetric Mn−O stretching mode is less pronounced. The luminescence band shapes for the transitions to the two orbital components of $^2E$ are strikingly different; the Huang−Rhys parameters for the bending-mode progressions obtained from fits of simulated band shapes to the experimental spectra are 1.3 and 3.7, respectively. This is due to weak E⊗*e* and stronger $T_2$⊗*e* Jahn−Teller (JT) effects in the ground and excited LF states, respectively. The linear vibronic coupling constants are $f_E \approx 180$ $cm^{-1}$ and $f_T \approx -730$ $cm^{-1}$ and the corresponding JT stabilization energies $E_{JT}(^2E) \approx 50$ $cm^{-1}$ and $E_{JT}(^2T_2) \approx 780$ $cm^{-1}$, respectively.

## 1. Introduction

Despite the simple $3d^1$ electron configuration of the $MnO_4^{2-}$ ion, the interpretation of the optical absorption spectra of nominally $MnO_4^{2-}$-doped $BaSO_4$ is inconsistent. In the first detailed study of the EPR and optical absorption spectra of Mn-doped $BaSO_4$ the single unpaired electron was found to occupy the $d_z^2$ orbital, where **z** lies in the $C_s$ mirror plane of the $SO_4^{2-}$ ion in $BaSO_4$.[1] In the spectral region above 16 500 $cm^{-1}$ the absorption spectra reported in ref 1 look very similar to those of $K_2SO_4$:$Mn^{6+}$ grown from a basic aqueous solution,[2] consisting of a series of intense ligand-to-metal charge transfer (LMCT) bands. In the red and near-infrared (near-IR), on the other hand, the spectra for the two systems are strikingly different. For $K_2SO_4$:$Mn^{6+}$ they consist of a highly structured weak band centered at 12 500 $cm^{-1}$ due to the $^2E \rightarrow {}^2T_2$ ligand-field (LF) transition of $MnO_4^{2-}$. In the spectra of Mn-doped $BaSO_4$ a group of weakly structured intense bands with a marked polarization dependence peak in the 10 000−16 500 $cm^{-1}$ region. They were tentatively assigned to LMCT transitions of $MnO_4^{2-}$ [1] and subsequently to the three orbital components of the $^2T_2$ LF state borrowing their high intensity from nearby LMCT states.[3]

Recently we reported the first luminescence spectra of $MnO_4^{2-}$ doped into various host lattices.[4,5] Luminescence is due to the $^2T_2 \rightarrow {}^2E$ LF transition, and at 10 K it consists of a broad structured band extending from about 11 000 to 7000 $cm^{-1}$. In the spectrum of Mn-doped $BaSO_4$ the $MnO_4^{2-}$ luminescence is superimposed by a much sharper feature at 8340 $cm^{-1}$. In contrast to the other Mn-doped systems which were all prepared by slowly evaporating basic aqueous solutions at room temperature, $BaSO_4$ is insoluble in water and manganese doped crystals were grown from a NaCl−KCl flux between 750 and 650 °C, according to ref 1. Driven by its potential as tunable solid-state laser material,[6] we engaged in a detailed spectroscopic investigation of Mn-doped $BaSO_4$. On the basis of a systematic study of the spectroscopic properties of $MnO_4^{3-}$ in a variety of hosts[7] and by combining absorption and luminescence data, we were able to show that under the preparation conditions described in ref 1 only half of the manganese is incorporated as $MnO_4^{2-}$, while the remainder enters as $MnO_4^{3-}$.[8] The assignment of the absorption bands between 10 000 and 16 500 $cm^{-1}$ to $^3A_2 \rightarrow {}^3T_2$, $^3T_1$ and the sharp-line emission to $^1E \rightarrow {}^3A_2$ (d → d) transitions of $MnO_4^{3-}$ was then relatively straightforward.[8]

In the present study we report on the preparation of manganese-doped single crystals of $BaSO_4$ which contain, in essence, $MnO_4^{2-}$. The low-temperature absorption and luminescence spectra are strongly polarized, thus allowing an unambiguous band assignment. The fine structure in the $^2E \leftrightarrow {}^2T_2$ LF spectra is analyzed in the framework of time-dependent theory of electronic spectroscopy. From fits of simulated band shapes to the experimental spectra we obtain the relative

[⊗] Abstract published in *Advance ACS Abstracts*, March 15, 1997.

(1) Kosky, C. A.; McGarvey, B. R.; Holt, S. L. *J. Chem. Phys.* **1972**, *56*, 5904.
(2) DiSipio, L.; Oleari, L.; Day, P. *J. Chem. Soc., Faraday Trans. 2* **1972**, *68*, 776.
(3) Borromei, R.; Oleari, L.; Day, P. *Phys. Status Solidi B* **1984**, *124*, 707.
(4) Brunold, T. C.; Hazenkamp, M. F.; Güdel, H. U. *J. Am. Chem. Soc.* **1995**, *117*, 5598.
(5) Brunold, T. C.; Güdel, H. U. *Chem. Phys. Lett.* **1996**, *249*, 77.
(6) Brunold, T. C.; Hazenkamp, M. F.; Güdel, H. U. In *OSA Trends in Optics and Photonics on Advanced Solid State Lasers*; Payne, S. A., Pollock, C. R., Eds.; Optical Society of America: Washington, DC, 1996; Vol. 1, p 474.
(7) Oetliker, U.; Herren, M.; Güdel, H. U.; Kesper, U.; Albrecht, C.; Reinen, D. *J. Chem. Phys* **1994**, *100*, 8656.
(8) Brunold, T. C.; Güdel, H. U. *Chem. Phys. Lett.* **1996**, *257*, 123.

S0020-1669(96)01171-8 CCC: $14.00 

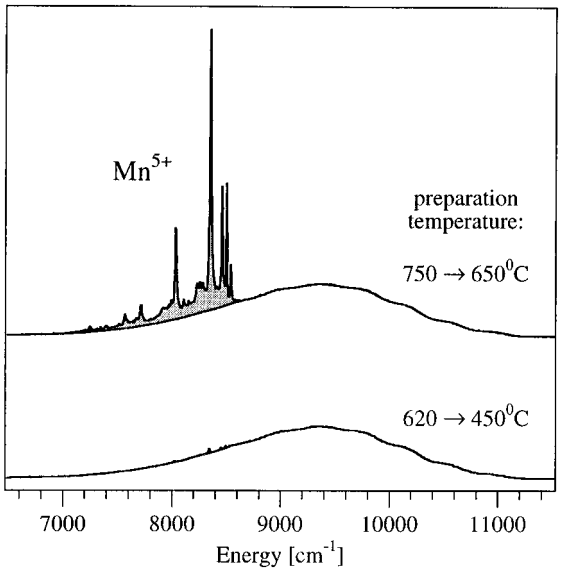


**Figure 1.** Unpolarized 100 K luminescence spectra of Mn-doped $BaSO_4$ crystals grown between 750 and 650 °C from a NaCl−KCl flux (upper curve) and between 620 and 450 °C from a NaCl−KCl−CsCl flux (lower curve). In the upper spectrum the broad band due to $^2T_2 \rightarrow {}^2E$ luminescence of $MnO_4^{2-}$ is superimposed by $^1E \rightarrow {}^3A_2$ sharp-line emission of $MnO_4^{3-}$ (shaded area).

displacements of the potential-energy surfaces of the initial and final states along bending and stretching coordinates. This permits us to determine the strengths of the Jahn−Teller (JT) effects in the ground and excited LF states of $MnO_4^{2-}$ in the $BaSO_4$ host. These results are compared with those reported recently for $Cs_2SO_4$: $Mn^{6+}$, where the unusually well-resolved fine structure in the $^2E \leftrightarrow {}^2T_2$ LF spectra has been analyzed quantitatively.[9]

## 2. Experimental Section

**2.1. Sample Preparation.** Single crystals of Mn-doped $BaSO_4$ were prepared by the flux method. In order to prevent the formation of $MnO_4^{3-}$ in the flux, the growth temperature must be kept below 620 °C.[10] Attempts with fluxes composed of two different alkali chlorides, with LiCl as the one component to establish a low melting point, failed due to the reduction of the initially introduced $KMnO_4$ to manganese-(IV). Therefore we switched to ternary alkali-metal chloride fluxes, and the system composed of NaCl, KCl, and CsCl proved to be suitable. Best results were obtained using the weight composition NaCl (13%), KCl (18%), CsCl (64%), and $BaSO_4$ (5%). $KMnO_4$ was added in concentrations of 0.1 or 0.5 mol % with respect to $BaSO_4$. Samples with the high Mn concentration were exclusively used to measure the weak (d → d) absorption in the near-infrared (near-IR) region. The starting materials were thoroughly mixed, fired for 12 h at 620 °C in a temperature controlled furnace, and cooled to 450 °C at −1.5 °C/h using platinum crucibles with tight-fitting lids. The size of the crystals is typically $3 \times 1.5 \times 1$ mm$^3$ along the crystallographic **b**, **c**, and **a** axes, respectively. Their color is pink, in contrast to the blue color of Mn-doped crystals of $BaSO_4$ containing similar amounts of $MnO_4^{2-}$ and $MnO_4^{3-}$. This appears to be the first $MnO_4^{2-}$-doped system which is not blue or green in color.

Figure 1 compares the unpolarized 100 K luminescence spectra of Mn-doped $BaSO_4$ prepared from a NaCl−KCl flux between 750 and 650 °C according to ref 1 (upper trace) and a sample grown between 620 and 450 °C (lower trace). The dominant $^1E \rightarrow {}^3A_2$ sharp-line luminescence of $MnO_4^{3-}$ below 8500 cm$^{-1}$ in the upper spectrum (shaded area) is weaker by more than 2 orders of magnitude in the lower spectrum. Hence, the $MnO_4^{2-}/MnO_4^{3-}$ ratio in the crystals used for the present study is larger than 100/1,[8] and all the relevant features in the spectra presented here are due to $MnO_4^{2-}$.

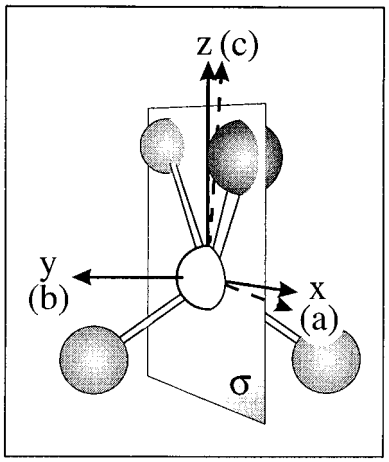


**Figure 2.** Schematic illustration of the $SO_4^{2-}$ ion in $BaSO_4$. The crystallographic and molecular axes are denoted by **a**, **b**, **c** and **x**, **y**, **z**, respectively. The only symmetry element of the sulfate ion is the mirror plane $\sigma$ perpendicular to **y**(**b**), but the symmetry is approximately $C_{2v}$, the **z** axis being the pseudo $C_2$ axis. Note that compared to the commonly used axes orientation the **x**, **y** axes are rotated by 45° around **z**.

**2.2. Absorption and Luminescence Measurements.** Absorption spectra in the vis and UV spectral region were recorded on a double-beam spectrometer (Cary 5e) fitted with a closed-cycle helium refrigerator (Air Products) for sample cooling to 10 K. High-resolution absorption spectra in the near-infrared (near-IR) region were measured on a home-built double-beam unit equipped with a red-sensitive PM tube (Hamamatsu R 406) and attached to a double monochromator (0.85 m Spex 1402). Samples were cooled to 15 K in a cold helium-gas stream. The light was polarized with **E** parallel to the crystallographic **a**/**b** and **b**/**c** axes of crystals polished perpendicular to **c** and **a**, respectively. The orientation of one of the four crystallographically equivalent $SO_4^{2-}$ ions in the orthorhombic unit cell of $BaSO_4$ is shown in Figure 2. The only symmetry element of the sulfate ion is a mirror plane ($\sigma$) perpendicular to **b**, and the site symmetry is thus $C_s$.[11] The angular deviations from a regular tetrahedron are substantial, leading to the strongly polarized optical spectra of $BaSO_4$:$Mn^{6+}$ presented in the following.

Broad band excitation of the luminescence was performed with a xenon lamp (Varian XBO 150 W/4) filtered by a saturated aqueous $Cu^{2+}$ solution and a color filter (Schott KG 4). The emitted light was dispersed by a single monochromator (3/4 m Spex 1702) equipped with a grating blazed at 1.25 $\mu$m and detected by a germanium detector (ADC 403 L, cooled with liquid $N_2$) in conjunction with a lock-in amplifier (SR 510). The spectra were corrected for system response. For lifetime measurements the samples were excited at 532 nm with the second harmonic of a pulsed YAG:Nd laser (Quanta-Ray DCR-3). Decay curves were recorded with a cooled PM tube (Hamamatsu R 3310) at 980 nm and stored with a multichannel scaler (SR 430). Variable sample temperatures between 10 and 300 K were achieved with a cold helium-gas flow technique.

## 3. Results

**3.1. Absorption Spectra.** The polarized 10 K absorption spectra of $BaSO_4$:$Mn^{6+}$ for **E** parallel to **a**, **b**, and **c** are shown in Figure 3. In the near-IR a weak band system extends from 11 074 cm$^{-1}$ (origin) to about 14 000 cm$^{-1}$ and exhibits a well-developed progression in **a** polarization. From a comparison with the absorption spectra of $K_2SO_4$:$Mn^{6+}$,[2] it is readily assigned to the $^2E \rightarrow {}^2T_2$ ligand-field (LF) transition of $MnO_4^{2-}$. The spectral region above 16 000 cm$^{-1}$ consists of four intense bands showing a marked polarization dependence. In $BaSO_4$

(9) Brunold, T. C.; Riley, M. J.; Güdel, H. U. *J. Chem. Phys.* **1996**, *105*, 7931.

(10) Booth, J. S.; Dallimore, D.; Heal, G. A. *Thermochim. Acta* **1980**, *39*, 281.

(11) Wyckoff, R. W. G. *Crystal Structures*, 2nd ed.; Interscience: New York, 1965; Vol. 3, p 45.

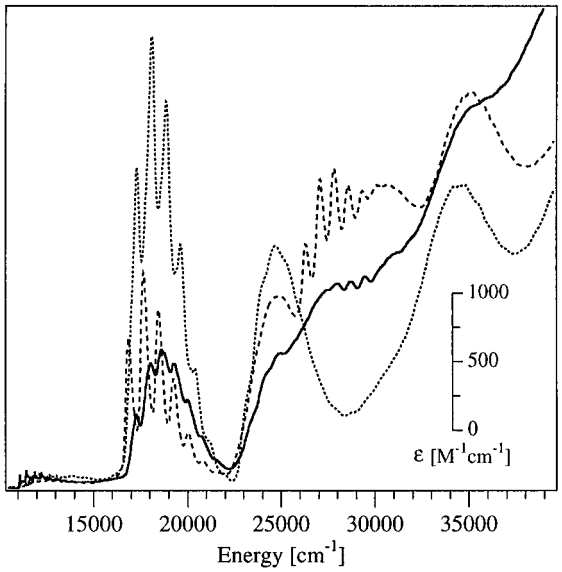


**Figure 3.** **E**||**a** (solid line), **E**||**b** (broken line), and **E**||**c** (dotted line) polarized absorption spectra of $BaSO_4$:$Mn^{6+}$ at 10 K.

**Table 1.** Spectral Positions of the Band Maxima $E_{max}$ and Vibrational Frequencies $\tilde{\nu}$ for Resolved Progressions for the Four Lowest-Energy LMCT Transitions of $MnO_4^{2-}$ in $BaSO_4$ (in $cm^{-1}$)[a]

| **E**\|\|**a** | | **E**\|\|**b** | | **E**\|\|**c** | | |
|---|---|---|---|---|---|---|
| $E_{max}$ | $\tilde{\nu}$ | $E_{max}$ | $\tilde{\nu}$ | $E_{max}$ | $\tilde{\nu}$ | assgnt |
| 18 700 | 730 | 18 100 | 790 | 18 300 | 780 | $^2E \rightarrow {}^2T_2$ |
| 24 750 | 750 | 24 650 | | 24 650 | 730 | $^2E \rightarrow {}^2T_2$ |
| 28 700 | 760 | 27 850 | 760 | absent | | $^2E \rightarrow {}^2T_1$ |
| 34 700 | | 35 000 | | 34 300 | | $^2E \rightarrow {}^2T_2$ |

[a] Band assignments are given in tetrahedral notation.

these bands are shifted to the blue compared to $K_2SO_4$:$Mn^{6+}$,[2] giving rise to the pink color of the title compound. Band positions together with vibrational frequencies for resolved progressions are listed in Table 1. Their assignment to ligand-to-metal charge transfer (LMCT) transitions of $MnO_4^{2-}$ is relatively straightforward and in accordance with earlier assignments.[1,3] Note that the band peaking at 28 000 $cm^{-1}$ is absent for **E**||**c**.

Figure 4 shows the **E**||**a**, **E**||**b**, and **E**||**c** polarized 15 K absorption spectra of $BaSO_4$:$Mn^{6+}$ in the region of the $^2E \rightarrow {}^2T_2$ LF transition. In $BaSO_4$ both the initial and final states are split by the combined action of the $C_s$ site perturbation[11] and spin−orbit coupling, and the spectra in Figure 4 are thus composed of three overlapping bands. The highly structured band with an origin at 11 074 $cm^{-1}$ appears in all three spectra but predominantly in **a** polarization. The origin of the second band peaks at 11 570 $cm^{-1}$ exclusively for **E**||**c**. The assignment of the small peak at 11 790 $cm^{-1}$ to the origin of the third band is made difficult by its presence in all three polarizations and its bandwidth far exceeding that of the other two origin lines. However, it is supported by the corresponding sideband structure which dominates the **E**||**b** spectrum. The positions of the three electronic origins I−III and their respective vibrational sidebands in O−Mn−O bending ($\delta$) modes with frequencies of about 340 $cm^{-1}$ and the totally symmetric Mn−O stretching ($\nu$) mode of ≈800 $cm^{-1}$ are indicated in the appropriate polarization. The progressions are dominated by bending modes whereas coupling to the stretching mode is less pronounced.

**3.2. Luminescence Spectra.** The **E**||**a**, **E**||**b**, and **E**||**c** polarized 20 K luminescence spectra of $BaSO_4$:$Mn^{6+}$ shown in Figure 5 consist of a strongly polarized band system with a maximum around 9300 $cm^{-1}$. It is readily assigned to $^2T_2 \rightarrow$

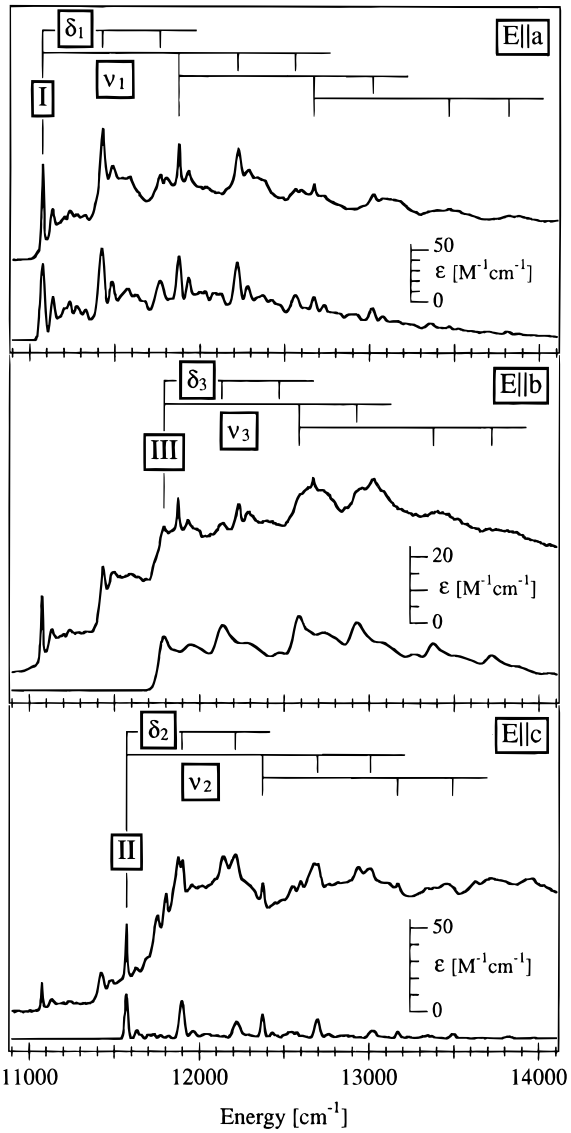


**Figure 4.** **E**||**a**, **E**||**b**, and **E**||**c** polarized 15 K absorption spectra of $BaSO_4$:$Mn^{6+}$ in the region of the $^2E \rightarrow {}^2T_2$ (d → d) transition (upper curves in each graph). Three electronic origins I−III and their respective progressions in bending ($\delta$) and stretching ($\nu$) modes are indicated. The lower curves show band shape simulations for the three transitions obtained with eq 1 and the parameters listed in Table 2.

$^2E$ of $MnO_4^{2-}$ from the coincidence of the origin line at 11 074 $cm^{-1}$ with origin I in absorption; see Figure 4. In the origin region of the **a** polarization it exhibits a rich fine structure, and it is twice as intense as for the other polarizations. In this region the **E**||**b** and **E**||**c** polarized spectra are very similar to each other, but below 10 700 $cm^{-1}$ they differ considerably. In **b** polarization the weakly structured band with a maximum at 9500 $cm^{-1}$ is about three times stronger than for **E**||**c**. This suggests that the luminescence spectra in Figure 5 are actually composed of two overlapping bands corresponding to the two components of the orbitally split ground state: (i) a highly structured mainly **a** polarized emission (*I*) originating at 11 074 $cm^{-1}$; (ii) an essentially **b** polarized poorly structured emission (*J*) with an origin around 10 700 $cm^{-1}$.

We attempted to resolve the band shapes of emissions *I* and *J* using the following approach. After scaling to equal intensity in the origin region of emission *I*, the **E**||**a** spectrum was subtracted from the **E**||**b** curve to generate a new spectrum corresponding, in essence, to emission *J*. This new spectrum was then appropriately scaled and subtracted from the **E**||**a**

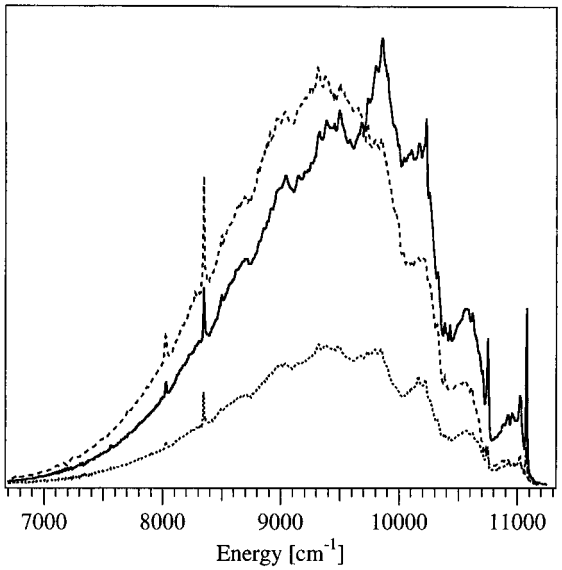


**Figure 5.** **E**||**a** (solid line), **E**||**b** (broken line), and **E**||**c** (dotted line) polarized 20 K luminescence spectra of $BaSO_4$:$Mn^{6+}$. The sharp lines below 8500 $cm^{-1}$ are due to $^1E \rightarrow {}^3A_2$ luminescence of small traces of $MnO_4^{3-}$.

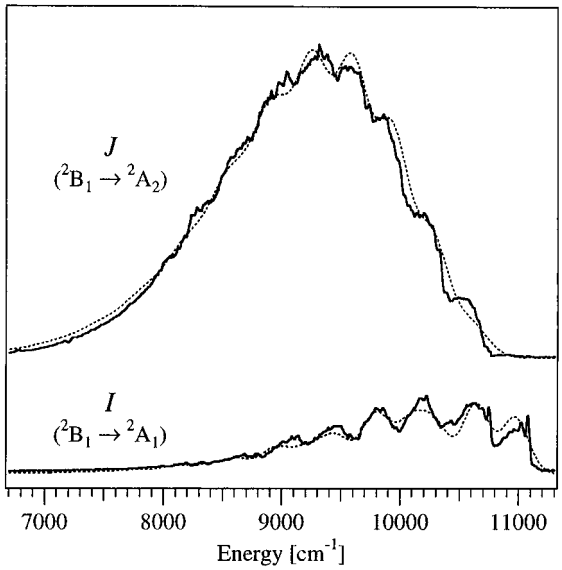


**Figure 6.** Resolved band shapes for emissions *I* and *J* at 20 K, lower and upper solid curves, respectively, obtained as described in section 3.2. The spectra are scaled according to the branching ratio. The dotted lines show the simulated band shapes obtained with eq 3 and the parameters listed in Table 3.

polarization to resolve the band shape of emission *I*. The resulting spectra for emissions *I* and *J* are shown in Figure 6, lower and upper solid lines, respectively. The band shapes of emission *I* and absorption I are very similar. The dominating progression-forming mode in emission is a bending mode of about 330 $cm^{-1}$. As in absorption, coupling to the totally symmetric stretching mode of 850 $cm^{-1}$ is less important. The band shape of emission *J* is strikingly different. The sideband structure is again dominated by bending-mode progressions, but the relative sideband intensity is much higher compared to emission *I*. This clearly indicates a sizable displacement of the two orbital components of the $^2E$ ground state relative to each other along the bending coordinates.

The luminescence lifetime of $MnO_4^{2-}$ in $BaSO_4$ at 10 K is 2.75 $\mu$s. Both lifetime and intensity are practically constant up to 100 K and then start dropping parallel to each other. At 300 K the lifetime is 650 ns and the intensity has decreased to 21% of its 10 K value.[5]

## 4. Discussion

**4.1. Site Symmetry in $BaSO_4$.** The only symmetry element of the sulfate ion in $BaSO_4$ is a mirror plane perpendicular to the crystallographic **b** axis,[11] and the site symmetry is thus $C_s$. The O−S−O angles vary between 105.9 and 114.1°, indicating a substantial distortion of the $SO_4^{2-}$ ion in the crystal structure. Yet, the $C_s$ site perturbation corresponds essentially to a $T_d \rightarrow C_{2v}$ distortion, and therefore we analyze the optical spectra of $MnO_4^{2-}$-doped $BaSO_4$ in the approximate $C_{2v}$ point group. The convention used for the orientation of the molecular **x**, **y**, **z** axes of S(Mn)$O_4^{2-}$ is illustrated in Figure 2. The **z** axis is the pseudo $C_2$ axis, bisecting the angle between the two oxygen atoms above and below the $C_s$ mirror plane ($\sigma$). Both the **x** and **z** axes lie in the **ac** ($\sigma$) plane. They are rotated by 8° from the **a** and **c** axes, respectively, while **y** coincides with **b**. The **a**, **b**, and **c** polarized crystal spectra in Figures 3−5 thus correspond essentially to the **x**, **y**, and **z** polarized molecular spectra.

The effect of the $T_d \rightarrow C_{2v}$ distortion on the $^2E \leftrightarrow {}^2T_2$ LF transitions of $MnO_4^{2-}$ is illustrated in Figure 7. Spin−orbit coupling is neglected because its effect is largely quenched by the crystal field. Both the ground and excited LF states split

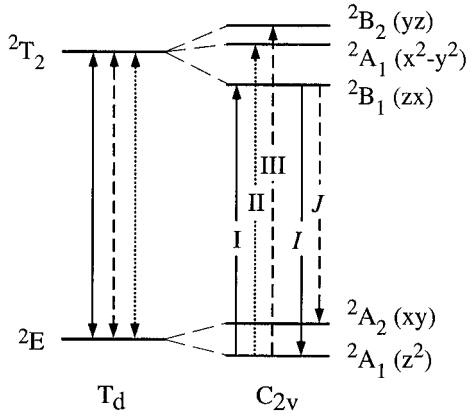


**Figure 7.** $T_d \rightarrow C_{2v}$ splitting of the ligand-field (LF) states of $MnO_4^{2-}$. The $C_{2v}$ transformation properties are given in brackets. The splitting patterns are based on the polarized spectra in Figures 4 and 5. Electric-dipole allowed transitions from the $^2A_1$ ground and $^2B_1$ emitting states are indicated by arrows: solid, broken, and dotted lines are **x**(**a**), **y**(**b**), and **z**(**c**) polarized, respectively. Designations of absorptions I−III and emissions *I* and *J* relate to Figures 4−6.

into their orbital components. From EPR it is known that the the single unpaired electron occupies the $d_z^2$ orbital,[1] and the ground state is thus $^2A_1(z^2)$. In $C_{2v}$ the components of the electric-dipole (*ed*) operator along **x**, **y**, and **z** transform as $B_1$, $B_2$, and $A_1$, respectively, giving rise to the selection rules shown by arrows in Figure 7: solid, broken, and dotted lines correspond to **x**(**a**), **y**(**b**), and **z**(**c**) polarized transitions, respectively.

In the tetrahedral approximation the highest-energy fully occupied set of molecular orbitals transforms as $t_1$ and is purely ligand centered. The states which arise from the $t_1^5e^2$ excited electron configuration thus formally correspond to ligand-to-metal charge transfer (LMCT) states. The corresponding spin doublet LMCT states transform either as $^2T_1$ or $^2T_2$. Upon $T_d \rightarrow C_{2v}$ distortion $^2T_1$ states split into the three orbital components $^2A_2$, $^2B_1$, and $^2B_2$. $^2A_1 \rightarrow {}^2A_2$ transitions are *ed* forbidden, and $^2T_1$ excitations are thus absent in **z**(**c**) polarization.

**4.2. $^2E \leftrightarrow {}^2T_2$ Ligand-Field Transitions. 4.2.1. Band Assignment.** The three electronic origins for the $^2E \rightarrow {}^2T_2$ ligand-field (LF) transition of $MnO_4^{2-}$ are indicated in the absorption spectra shown in Figure 4. On the basis of the

selection rules sketched in Figure 7 we can assign them to the orbital components of $^2T_2$. Absorption I is predominantly **a**(**x**) polarized and thus assigned to $^2A_1(z^2) \rightarrow {}^2B_1(zx)$. Absorption II is exclusively **c**(**z**) polarized and consequently due to $^2A_1(z^2) \rightarrow {}^2A_1(x^2 - y^2)$. Absorption III, which dominates the **b**(**y**) polarized spectrum, corresponds to $^2A_1(z^2) \rightarrow {}^2B_2(yz)$. The splitting pattern of $^2T_2$ derived from Figure 4 is sketched in Figure 7. Accordingly, luminescence originates at $^2B_1(zx)$ and emissions *I* and *J* are **a**(**x**) and **b**(**y**) polarized, respectively. This is in agreement with the observed polarization behavior; see Figure 5.

We have performed a crystal-field analysis in terms of the angular overlap model (AOM) of the $^2E \leftrightarrow {}^2T_2$ LF spectra in Figures 4 and 5. Using the $SO_4^{2-}$ host tetrahedron geometry we obtain splitting patterns for the ground and excited LF states which are consistent with the ordering of the levels in Figure 7. The orbital splittings are thus correlated with structural distortions of the $MnO_4^{2-}$ unit in $BaSO_4$. This is different in the $Cs_2SO_4$ host where the low-symmetry term in the crystal-field potential at the $Mn^{6+}$ site mainly arises from the second-nearest neighbor $Cs^+$ ions.[9]

The partial presence of the three $^2T_2$ excitations in all three polarizations of Figure 4 shows that the selection rules sketched in Figure 7 are slightly relaxed. This is due to some mixing of the components of $^2E$ and $^2T_2$ and can be explained in terms of (i) spin−orbit coupling because all the doublet states transform as $\Gamma_5$ in the double group of $C_{2v}$, (ii) the additional $C_{2v} \rightarrow C_s$ site distortion since both the $^2B_1$ and $^2A_1$ components become $^2A'$, while $^2A_2$ and $^2B_2$ become $^2A''$, and (iii) the Jahn−Teller effect in the ground state, see section 4.2.3.

The separation of the two origins of emissions *I* and *J* in Figure 6 is about 350 $cm^{-1}$. This is the splitting of the $^2E$ ground state. Values of 540 $cm^{-1}$ [12] and 290 $cm^{-1}$ [13] had been derived by indirect methods from EPR studies.

**4.2.2. Band Shape Analysis.** We now turn to a detailed analysis of the band shapes observed for the $^2E \leftrightarrow {}^2T_2$ LF transitions of $MnO_4^{2-}$ in $BaSO_4$. The fine structure in Figures 4 and 5 is less resolved than in the spectra of $Cs_2SO_4:Mn^{6+}$.[5,9] This can be explained in terms of the differing rigidity of the $BaSO_4$ and $Cs_2SO_4$ host lattices which both crystallize in the orthorhombic space group *Pnma*.[11] The oxygen atoms of $SO_4^{2-}$ are in close contact with the $Ba^{2+}$ and $Cs^+$ ions. In $BaSO_4$ the $Ba^{2+}$ ion has a rather compact coordination consisting of twelve oxygen atoms, eight of which are separated by less than 3 Å.[11] In $Cs_2SO_4$, on the other hand, the $Cs^+$ ions are surrounded by either eleven or nine oxygen atoms with average Cs−O distances of 3.3 and 3.2 Å, respectively.[14] Hence, when $MnO_4^{2-}$ substitutes for the substantially smaller $SO_4^{2-}$ unit, the nearby $Ba^{2+}$ ions are less flexible to accommodate the guest than $Cs^+$ and coupling between electronic transitions and lattice modes is stronger in $BaSO_4$.

Due to this strong electron−phonon coupling in $BaSO_4$ it is more difficult than in $Cs_2SO_4$ [9] to determine accurate Huang−Rhys parameters *S* for the progressions in the bending and stretching modes of $MnO_4^{2-}$ from the spectra in Figures 4 and 6. *S* is defined by the intensity ratio of the first sideband to the respective origin line, and it is related to the displacement $\Delta$ of the potential-energy surfaces of the initial and final states by $S = \Delta^2/2$. The approach used here is to determine $\Delta$ directly by fitting the experimental spectra with band shapes calculated in the framework of time-dependent theory of electronic spectroscopy.

**Table 2.** Origin Positions and Vibrational Frequencies of the Progression-Forming O−Mn−O Bending ($\delta$) and Mn-O Stretching ($\nu$) Modes for the $^2E \rightarrow {}^2T_2$ Ligand-Field Transition of $MnO_4^{2-}$ in $BaSO_4$[a]

| | absorption I $^2A_1 \rightarrow {}^2B_1$ | absorption II $^2A_1 \rightarrow {}^2A_1$ | absorption III $^2A_1 \rightarrow {}^2B_2$ |
|---|---|---|---|
| origin ($cm^{-1}$) | 11 074 | 11 570 | 11 790 |
| $\hbar\omega_\delta$ ($cm^{-1}$) | 345 | 325 | 345 |
| $\Delta_\delta$ | 1.55 | 1.55 | 1.30 |
| $S_\delta$ | 1.20 | 1.20 | 0.85 |
| $\hbar\omega_\nu$ ($cm^{-1}$) | 798 | 800 | 795 |
| $\Delta_\nu$ | 1.10 | 0.95 | 1.30 |
| $S_\nu$ | 0.60 | 0.45 | 0.85 |
| $10^6 f$(**E**\|\|**a**) | 560 | 0 | 121 |
| $10^6 f$(**E**\|\|**b**) | 151 | 0 | 204 |
| $10^6 f$(**E**\|\|**c**) | 86 | 26 | 368 |
| $10^6 f_{av}$ | 265 | 9 | 231 |

[a] The relative displacements $\Delta$, Huang−Rhys parameters *S*, and oscillator strengths *f* were obtained from fits of band shapes calculated using eq 1 to the experimental curves in Figure 4. Band designations are given in $C_{2v}$ notation.

Using the formalism of ref 15 the intensity distribution is given by

$$I(\omega) = C\omega \int_{-\infty}^{\infty} \exp(i\omega t)\langle\phi|\phi(t)\rangle \, dt \qquad (1)$$

$I(\omega)$ is the intensity in photons absorbed per unit time at frequency $\omega$, *C* is a constant, and the wavepacket overlap $\langle\phi|\phi(t)\rangle$ is given by

$$\langle\phi|\phi(t)\rangle = \exp\left(\sum_k \left[-\frac{\Delta_k^2}{2}(1 - \exp(-i\omega_k t)) - \frac{i\omega_k t}{2}\right] - iE_0 t - \Gamma^2 t^2\right) \qquad (2)$$

$\omega_k$ and $\Delta_k$ are the vibrational frequency and dimensionless displacement of the *k*th normal mode, respectively, $E_0$ is the energy of the zero-phonon transition, and $\Gamma$ is a damping factor which governs the width of the vibronic lines.

The emission spectrum, as distinct from the absorption spectrum, is proportional to $\omega^3$:[15]

$$I(\omega) = C'\omega^3 \int_{-\infty}^{\infty} \exp(i\omega t)\langle\phi|\phi(t)\rangle \, dt \qquad (3)$$

In the case of the $^2E \rightarrow {}^2T_2$ absorption spectra shown in Figure 4 the strong polarization dependence of the three transitions provides a suitable basis for band shape simulations. The simulated spectra for absorptions I−III obtained from fits of eq 1 to the experimental curves are plotted in Figure 4 at the bottom of the appropriate graph, and the corresponding fit parameters for the bending ($\delta$) and stretching ($\nu$) mode progressions are listed in Table 2. The increasing line width of the sidebands toward higher energies in the experimental spectra was simulated by cumulating a series of calculated spectra with slightly different $\delta$ vibrational frequencies according to a Gaussian distribution. The most informative simulation is for transition I in the **E**||**a** spectrum of Figure 4. This is the best resolved spectrum, and the simulation is seen to be remarkably good. Table 2 includes the oscillator strengths *f* of absorptions I−III in each polarization. These were obtained from decompositions of the experimental curves in Figure 4 into linear combinations of the simulated spectra.

(12) Ezzeh, C.; McGarvey, B. R. *J. Chem. Phys.* **1974**, *61*, 2675.
(13) Greenblatt, M.; Pifer, J. H. *J. Chem. Phys.* **1980**, *72*, 529.
(14) Nord, A. G. *Acta Chem. Scand.* **1976**, *30*, 198.
(15) Zink, J. I.; Kim Shin, K. S. In *Advances in Photochemistry*; Volman, D. H., Hammond, G. S., Neckers, D. C., Eds.; John Wiley & Sons, Inc.: New York, 1991; Vol. 16, p 119.

**Table 3.** Origin Positions and Vibrational Frequencies of the Progression-Forming $\delta$ and $\nu$ Modes for $^2T_2 \rightarrow {}^2E$ Emission of $MnO_4^{2-}$ in $BaSO_4$[a]

| | emission *I* $^2B_1 \rightarrow {}^2A_1$ | emission *J* $^2B_1 \rightarrow {}^2A_2$ | | emission *I* $^2B_1 \rightarrow {}^2A_1$ | emission *J* $^2B_1 \rightarrow {}^2A_2$ |
|---|---|---|---|---|---|
| origin ($cm^{-1}$) | 11 074 | ≈10 720 | $S_\nu$ | 0.8 | 0.5 |
| $\hbar\omega_\delta$ ($cm^{-1}$) | 330 | 330 | $I$(**E**\|\|**a**) | 1.67 | 5.24 |
| $\Delta_\delta$ | 1.6 | 2.7 | $I$(**E**\|\|**b**) | 0.71 | 6.61 |
| $S_\delta$ | 1.3 | 3.7 | $I$(**E**\|\|**c**) | 0.62 | 1.98 |
| $\hbar\omega_\nu$ ($cm^{-1}$) | 850 | 800 | $I_{av}$ | 1.00 | 4.61 |
| $\Delta_\nu$ | 1.3 | 1.0 | | | |

[a] The relative displacements $\Delta$, Huang−Rhys parameters $S$, and intensities $I$ (in arbitrary units) were obtained from fits of band shapes calculated with eq 3 to the experimental curves in Figure 6. $C_{2v}$ notation is used for band designations.

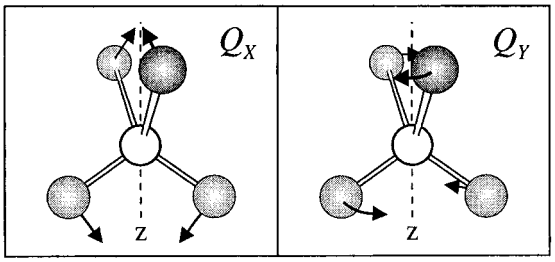


**Figure 8.** Illustration of the two components $Q_X$ and $Q_Y$ of the *e* bending mode in a tetrahedral $MO_4$ complex.

The relevant parameters obtained from fits of simulated band shapes to emissions *I* and *J* in Figure 6 are listed in Table 3. The simulated spectra are plotted as dotted lines on top of the experimental curves in Figure 6. The good correspondence between the simulated and experimental spectra supports our approach for the band shape isolation described in section 3.2.

By inspection of Tables 2 and 3 we note that the Huang−Rhys parameter $S_\delta$, in contrast to $S_\nu$, varies considerably; it ranges from 0.85 (absorption III) to 3.7 (emission *J*). This indicates sizable displacements of the $^2E$ and $^2T_2$ potentials along the bending coordinates. In refs 16 and 17 the dominance of bending-mode progressions in the $^2E \rightarrow {}^2T_2$ LF absorption spectra of $MnO_4^{2-}$ in various alkali metal sulfate hosts was associated with the possibility of Jahn−Teller (JT) distortions. Recently, the fine structure in the $^2E \leftrightarrow {}^2T_2$ LF spectra of $MnO_4^{2-}$ in $Cs_2SO_4$ was analyzed quantitatively and both the ground and excited LF states were found to be subject to JT interactions with the *e* bending mode.[9] In analogy to $BaSO_4$ the $SO_4^{2-}$ site symmetry in $Cs_2SO_4$ is reduced to $C_s$, and therefore we analyze the $^2E \leftrightarrow {}^2T_2$ LF spectra of $BaSO_4$:$Mn^{6+}$ using the same approach. However, because of the insufficiently resolved fine structure we do not attempt here to determine the JT parameters by fitting the $^2T_2 \rightarrow {}^2E$ emission spectrum in terms of a vibronic Hamiltonian including JT coupling terms.

**4.2.3. Jahn−Teller Effects in the $^2E$ and $^2T_2$ Ligand-Field States.** Let us first consider E⊗*e* vibronic coupling in the ground state. The two components of the *e* bending mode, $Q_X$ (transforming as $z^2$) and $Q_Y$ (transforming as *xy* for the axes orientation in Figure 2), are depicted in Figure 8. The vibronic Hamiltonian $H$ is that of the usual E⊗*e* problem, $H_{JT}$, with an additional term $H_{CF}$ to account for the noncubic crystal-field (CF) potential in $BaSO_4$, which formally makes this a pseudo-JT problem. $H_{CF}$ destroys the cubic symmetry of the Hamiltonian; i.e., terms which are equivalent by symmetry in the cubic limit become inequivalent. However, in order to avoid a hopelessly overparametrized problem, one usually makes the approximation that symmetry-equivalent terms in the original Hamiltonian remain so even when the symmetry is lowered. The vibronic Hamiltonian to first order for the diabatic electronic basis of the ground state, $\psi_x \sim z^2$ and $\psi_y \sim xy$, can then be written as[18]

$$H = H_0 + H_{JT} + H_{CF} \tag{4}$$

where

$$\frac{H_0}{\hbar\omega_e} = \frac{1}{2}\left(-\frac{\partial^2}{\partial X^2} - \frac{\partial^2}{\partial Y^2} + X^2 + Y^2\right)\begin{pmatrix}1 & 0\\ 0 & 1\end{pmatrix} \tag{4a}$$

$$\frac{H_{JT}}{\hbar\omega_e} = F_E\begin{pmatrix}X & -Y\\ -Y & -X\end{pmatrix} \tag{4b}$$

$$\frac{H_{CF}}{\hbar\omega_e} = \begin{pmatrix}S_X & -S_Y\\ -S_Y & -S_X\end{pmatrix} \tag{4c}$$

*X*,*Y* are the coordinates of the *e* vibration $Q_X$,$Q_Y$ made dimensionless and $F_E$ is the linear Jahn−Teller coupling constant $f_E$ in units of the vibrational frequency $\hbar\omega_e = 330$ $cm^{-1}$ (see Table 3). From a theoretical study of the JT effect in tetrahedral $d^1$ systems it is known that $F_E$ is positive.[19] $S_X$ and $S_Y$ are the two components of the noncubic CF potential in $BaSO_4$ transforming as $z^2$ and *xy*, respectively. In the cubic limit they describe static distortions of the $MnO_4^{2-}$ ion along $Q_X$ and $Q_Y$, respectively.

For a cubic JT system the Hamiltonian comprises only terms (4a) and (4b), and the adiabatic potential-energy surface (APS) takes the form of the well-known "Mexican hat".[20] The effect

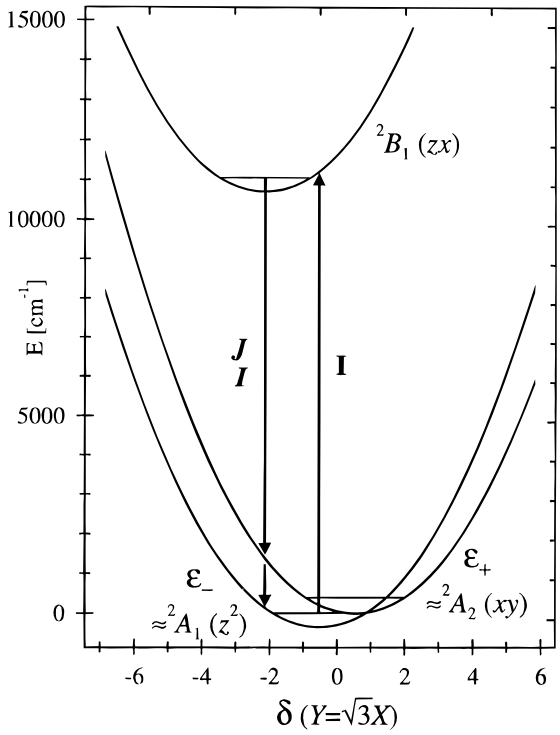


**Figure 9.** Cut through the potential-energy surfaces of $\epsilon_-$, $\epsilon_+$, and $^2B_1$ in *X*,*Y* coordinate space along $\delta$, i.e. $Y = \sqrt{3}X$. Designations of absorption I and emissions *I* and *J* relate to Figures 4−6.

(16) Day, P.; DiSipio, L.; Oleari, L. *Chem. Phys. Lett.* **1970**, *5*, 533.
(17) Day, P.; DiSipio, L.; Ingletto, G.; Oleari, L. *J. Chem. Soc., Dalton Trans.* **1973**, 2595.
(18) Riley, M. J.; Hitchman, M. A.; Mohammed, A. W. *J. Chem. Phys.* **1987**, *87*, 3766.
(19) Agresti, A.; Ammeter, J. H.; Bacci, M. *J. Chem. Phys.* **1984**, *81*, 1861.
(20) Bersuker, I. B. *The Jahn−Teller Effect and Vibronic Interactions in Modern Chemistry*; Plenum: New York, 1984; p 52.

of the low-symmetry term (4c) is to lift the degeneracy of the diabatic electronic functions $\psi_x$ and $\psi_y$. If this term is large compared to the JT effect, we obtain an energy surface which consists of two isolated parabolas $\epsilon_-$ and $\epsilon_+$. The positions of their minima in $X,Y$ space are related by inversion at $X = Y = 0$. These parabolas correspond to the slightly perturbed potentials of $^2A_1(\psi_x \sim z^2)$ and $^2A_2(\psi_y \sim xy)$, the energy ordering being given by the sign of $S_X$. In that case the emission spectrum shows two overlapping bands due to the transitions to $\epsilon_+$ and $\epsilon_-$, just as we observe for $BaSO_4$:$Mn^{6+}$; see Figure 6.

The Jahn−Teller active modes in the $^2T_2$ state are the $e$ and $t_2$ bending and $t_2$ stretching modes. A theoretical study of JT effects in T states in terms of the AOM suggests that coupling to the $e$ mode is dominant.[21] This is in accordance with experimental results on tetrahedrally coordinated $Cu^{2+}$ ($^2T_2$ ground state) in $ZnCr_2O_4$[22] and various tetrachlorocuprates(II)[23] and on $Cs_2SO_4$: $Mn^{6+}$.[9] We will hence restrict ourselves to the T⊗$e$ problem, for which the Hamiltonian for the electronic basis $\psi_\xi \sim yz$, $\psi_\eta \sim zx$, and $\psi_\zeta \sim x^2 - y^2$ takes the simple form[20]

$$\frac{H_{JT}}{\hbar\omega'_e} = F_T \begin{pmatrix} -{}^1/_2X + \frac{\sqrt{3}}{2}Y & 0 & 0 \\ 0 & -{}^1/_2X - \frac{\sqrt{3}}{2}Y & 0 \\ 0 & 0 & X \end{pmatrix} \qquad (5)$$

where $\hbar\omega'_e = 340$ cm$^{-1}$ is the vibrational frequency of the $e$ mode in the $^2T_2$ state (Table 2) and $F_T$ denotes the linear vibronic constant in units of $\hbar\omega'_e$. The adiabatic potential-energy surface consists of a set of three equivalent parabolas in $X,Y$ space, intersecting at the point $X = Y = 0$.[20] The electronic wave functions for the three parabolas are mutually orthogonal and are mixed neither by tetragonal displacements nor by distortions along $Q_X$,$Q_Y$. The effect of such distortions is to lift the electronic degeneracy of $^2T_2$, which leads to an absorption spectrum consisting of three overlapping Poissonian-like bands with harmonic progressions in the $e$ mode.

Simultaneous distortions of a regular tetrahedron along $Q_X$ and $Q_Y$ lower the symmetry to $D_2$, while $MnO_4^{2-}$ occupies a site of $C_s$ symmetry in $BaSO_4$. In order to appropriately describe this $C_s$ distortion in terms of the parameters $S_X$ and $S_Y$ in (4c) we first consider its effect on $^2T_2$. In section 4.2.1 we showed that $^2B_1(\psi_\eta \sim zx)$ is the lowest-energy component of $^2T_2$. From eq 5 it follows that the position of the minimum of the potential corresponding to $^2B_1$ in $X,Y$ space is

$$\left({}^1/_2F_T, \frac{\sqrt{3}}{2}F_T\right) \qquad (6)$$

For tetrahedral $d^1$ complexes the vibronic constant $F_T$ is negative.[19] The minimum of $^2B_1$ is thus at negative $X,Y$ coordinates, its $Y$ coordinate being $Y = \sqrt{3}X$ (see eq 6). The $^2A_1(\psi_\zeta \sim x^2 - y^2)$ and $^2B_2(\psi_\xi \sim yz)$ components of $^2T_2$ are at similar energies and clearly above $^2B_1$ (see Figure 7), demonstrating that the $BaSO_4$ host favors a static distortion of the $MnO_4^{2-}$ dopant as it occurs in the $^2B_1$ state. This is a distortion along $-Q_X$ and $-Q_Y$, see eq 6, suggesting that the strain parameters $S_X$ and $S_Y$ in the low-symmetry term (4c) are both negative. Moreover, from the position of the minimum of $^2B_1$ we conclude that $S_Y \approx \sqrt{3}S_X$, and we set $S_Y = \sqrt{3}S_X$. Physically this means that we orient the three minima of the potentials corresponding to $^2B_1$, $\epsilon_-$, and $\epsilon_+$ on a straight line $\delta$ in $X,Y$ space, and we will thus obtain lower and upper limits for the strength of the JT effects in the ground and excited LF states, respectively. This line is given by $Y = \sqrt{3}X$; see eq 6. The minimum of $\epsilon_-$ is adjacent to that of $^2B_1$, i.e. at negative $X$ and $Y$ coordinates. Figure 9 shows a cut through the potential-energy surfaces of $\epsilon_-$, $\epsilon_+$, and $^2B_1$ along $\delta$. The $X,Y$ coordinates of the minima of $\epsilon_-$ and $\epsilon_+$ are respectively (see eq 4):

$$\left(-{}^1/_2\left|F_E\right|, -\frac{\sqrt{3}}{2}\left|F_E\right|\right), \left({}^1/_2\left|F_E\right|, \frac{\sqrt{3}}{2}\left|F_E\right|\right) \qquad (7)$$

and their displacement along $\delta$ is thus $2F_E$.

On the basis of the band shape simulations for emissions $I$ and $J$ discussed in section 4.2.2, we obtained $\Delta_\delta$ values of 1.6 and 2.7 for the relative displacements along $\delta$ of the $^2B_1$ emitting level from the two components of the ground state $\epsilon_- \approx {}^2A_1(z^2)$ and $\epsilon_+ \approx {}^2A_2(xy)$, respectively (see Table 3 and Figure 9). Hence, we get $2F_E = 1.1$ and $f_E = F_E \cdot \hbar\omega_e = 180$ cm$^{-1}$. The displacement of the minimum of the potential corresonding to $^2B_1$ from $X = Y = 0$ is equal to $|F_T|$, (see eq 6), and we find $F_T = -2.15$ and $f_T = F_T \cdot \hbar\omega'_e = -730$ cm$^{-1}$. We can now calculate the JT stabilization energies ($E_{JT}$) for the $^2E$ and $^2T_2$ LF states using the following expressions:[20]

$$E_{JT}(^2E) = \frac{F_E^{\,2}}{2}\hbar\omega_e = 50 \text{ cm}^{-1} \qquad (8a)$$

$$E_{JT}(^2T_2) = \frac{F_T^{\,2}}{2}\hbar\omega'_e = 780 \text{ cm}^{-1} \qquad (8b)$$

Table 4 offers a comparison of the Jahn−Teller parameters obtained for $MnO_4^{2-}$ in the two host lattices $BaSO_4$ and $Cs_2SO_4$.[9] The JT effect in the ground state is stronger in $BaSO_4$ than in $Cs_2SO_4$, while the opposite is true for $^2T_2$. We attribute this difference to the different splittings of the LF states due to the noncubic crystal-field potential which quench the Jahn−Teller effects. The $^2E$ splittings in $BaSO_4$ and $Cs_2SO_4$ are ≈350 and 969 cm$^{-1}$, respectively, while the $^2T_2$ splittings are about 715 and 300 cm$^{-1}$, respectively (see Table 4).

**Table 4.** Jahn−Teller Parameters and Orbital Splittings (‡$E$) for the $^2E$ and $^2T_2$ Ligand-Field States of $MnO_4^{2-}$ in $BaSO_4$ and $Cs_2SO_4$ (from ref 9) in cm$^{-1}$ Units

| | $BaSO_4$ | $Cs_2SO_4$ | | $BaSO_4$ | $Cs_2SO_4$ |
|---|---|---|---|---|---|
| $f_E$ | 180 | 91 | $f_T$ | −730 | −790 |
| $E_{JT}(^2E)$ | 50 | 14 | $E_{JT}(^2T_2)$ | 780 | 925 |
| ‡$E(^2E)$ | 350 | 969 | ‡$E(^2T_2)$ | 715 | 300 |

The fact that the JT effect in the ground state is much weaker than in the excited LF state is due to the different antibonding character of the e and $t_2$ molecular orbitals, which is of $\pi$ and $\sigma + \pi$ type for e and $t_2$, respectively. In analogy to $MnO_4^{2-}$, the JT effect in the $^2E$ ground state of the isoelectronic $VCl_4$ complex was found to be very weak; i.e., $E_{JT}(^2E)$ is smaller than 100 cm$^{-1}$.[24,25] For the $^2T_2$ ground state of $Cu^{2+}$ in $Cs_2CuCl_4$ ($3d^9$ with a hole in the $t_2$ shell), on the other hand, the JT stabilization energy is $E_{JT}(^2T_2) \approx 1200$ cm$^{-1}$ and thus strong enough to produce substantial static distortions of the $CuCl_4^{2-}$ unit.[26] The larger value of $E_{JT}(^2T_2)$ for $CuCl_4^{2-}$ than for

(21) Ceulemans, A.; Beyens, D.; Vanquickenborne, L. G. *J. Am. Chem. Soc.* **1984**, *106*, 5824.
(22) Reinen, D.; Atanasov, M.; Nikolov, G. S.; Steffens, F. *Inorg. Chem.* **1988**, *27*, 1678.
(23) Smith, D. W. *Coord. Chem. Rev.* **1976**, *21*, 93.
(24) Bacci, M. *Chem. Phys. Lett.* **1978**, *58*, 537.
(25) Parameswaran, T.; Konongstein, J. A.; Haley, L. V. *J. Mol. Spectrom.* **1977**, *66*, 350.
(26) Bacci, M. *J. Chem. Phys. Solids* **1980**, *41*, 1267.

$MnO_4^{2-}$ is mainly the result of the smaller force constant for the *e* bending mode in the copper system.

In section 4.2.1 we mention the JT effect as a possible source of the polarization mixing observed in the $^2E \leftrightarrow {}^2T_2$ LF spectra. In the present case E⊗*e* vibronic coupling causes a small admixture of $^2A_2(xy)$ to $^2A_1(z^2)$, and absorptions I and III become slightly allowed in **c**(**z**) and **a**(**x**) polarizations, respectively. Since $^2A_2 \rightarrow {}^2A_1$ is electric-dipole forbidden, this coupling does not affect absorption II. It is interesting to note that in the spectra of Figure 4 absorption II, in contrast to absorptions I and III, appears in a single polarization, i.e. for **E**||**c**(**z**).

In analogy to $Ti^{3+}$-doped sapphire[27] the large bandwidth of the $^2E \leftrightarrow {}^2T_2$ LF transitions of $MnO_4^{2-}$ results from simultaneous distortions along JT and totally symmetric coordinates. We feel that for efficient design and improvement of laser materials it is necessary to first study and understand in detail their optical spectroscopic properties.

**4.2.4. Temperature Dependence and Quantum Yield of the $^2T_2 \rightarrow {}^2E$ Emission.** The temperature independence of the $^2T_2 \rightarrow {}^2E$ luminescence intensity and lifetime of $MnO_4^{2-}$ in $BaSO_4$ below 100 K suggests that nonradiative relaxation processes from $^2T_2$ are negligible at low temperatures. However, the isoelectronic $CrO_4^{3-}$ ion in various hosts shows similar characteristics, although the quantum yield at 15 K is only about 3% or less.[28] Hence, we must compare the measured 10 K lifetime of 2.75 $\mu$s with the radiative lifetime $\tau_{rad}$ which can be calculated from the oscillator strength *f* of the corresponding absorption using[29]

$$\tau_{rad} = k_0 \frac{{\lambda_0}^2}{n[(n^2+2)/3]^2} \frac{g_u}{g_l} \frac{1}{f} \qquad (9)$$

$k_0$ is a constant ($1.5 \times 10^4$ s m$^{-2}$), $\lambda_0$ is the average emission wavelength ($1.07 \times 10^{-6}$ m), *n* is the refractive index averaged over all polarizations (1.64 [30]), and $g_u$,$g_l$ are the degeneracies of the upper (2) and lower (2) states, respectively. With $f_{av} = 265 \times 10^{-6}$ for absorption I (Table 2) we obtain $\tau^I_{rad} = 16.2$ $\mu$s for the radiative lifetime of emission *I*. Emission *J* is about 4.6 times stronger than emission *I*, (see Table 3), and $\tau^J_{rad}$ is thus 3.5 $\mu$s. Relaxation from the $^2B_1$ emitting level occurs via both emissions *I* and *J*. Therefore the radiative lifetime of $^2B_1$ is given by $(\tau_{rad})^{-1} = (\tau^I_{rad})^{-1} + (\tau^J_{rad})^{-1}$ and we obtain $\tau_{rad} = 2.9$ $\mu$s. This is in excellent agreement with the experimental value of 2.75 $\mu$s at 10 K, demonstrating that the quantum yield is unity at low temperatures.

**4.3. Ligand-to-Metal Charge Transfer Transitions.** On the basis of the $C_{2v}$ selection rules (see section 4.1), we assign the three ligand-to-metal charge transfer (LMCT) bands centered at 18 400, 24 700, and 34 700 cm$^{-1}$ peaking in all three polarizations to $^2T_2$ excitations. The band at 28 000 cm$^{-1}$ is absent in **c**(**z**) polarization and thus assigned to $^2E \rightarrow {}^2T_1$. The fact that the first LMCT band centered at 18 400 cm$^{-1}$ is due to $^2E \rightarrow {}^2T_2$ is easily understood. As a result of Coulomb interaction in the $e^2$ subshell, the lowest-energy component is $^3A_2$, and the resulting spin doublet LMCT state is $^2T_2$.

In **b** and **c** polarizations that LMCT band exhibits a well-developed vibrational progression in the Mn−O stretching mode; see Figure 3. This allows an estimate of the Mn−O bond length increase $\Delta r$ upon $^2T_2$ LMCT excitation. In the harmonic approximation $\Delta r$ is given by

$$\Delta r = {}^1/_2 \Delta Q_\nu = {}^1/_2 \sqrt{\frac{S_\nu \hbar}{\pi c \tilde{\nu} \mu}} \qquad (10)$$

$S_\nu$ and $\tilde{\nu}$ are the Huang−Rhys parameter and vibrational frequency (in cm$^{-1}$) for the progression in the totally symmetric stretching mode, respectively, and $\mu$ is the reduced mass which, for that mode, corresponds to the oxygen mass.[31] From fits of band shapes calculated using eq 1 to the experimental **E**||**b** and **E**||**c** curves we obtain respectively $S_\nu = 1.53$ and 1.62, and thus $\Delta r = 0.045$ and 0.047 Å. This is comparable with $S_\nu = 1.71$ and $\Delta r = 0.048$ Å for the lowest-energy $^1A_1 \rightarrow {}^1T_2$ LMCT transition of $MnO_4^-$.[32]

The lowest-energy allowed LMCT transition of $CrO_4^{2-}$ is $^1A_1 \rightarrow {}^1T_2$, it peaks around 27 000 cm$^{-1}$ in the $3CdSO_4 \cdot 8H_2O$ host.[33] This is about 8500 cm$^{-1}$ higher than the first LMCT transition of $MnO_4^{2-}$, although both the manganese and chromium ions carry the same formal charge in these complexes. On the basis of a simple Coulomb interaction picture, one would rather expect a lower transition energy for $CrO_4^{2-}$ because of its empty e shell. However, the experimental finding is qualitatively understood by the following considerations. The excited $t_1^5e^1$ electron configuration of the chromate ion gives rise to two spin singlet states $^1T_1$ and $^1T_2$. The lower-energy transition is to $^1T_1$, but it is symmetry forbidden and appears only as a weak shoulder at 24 100 cm$^{-1}$. The energy difference between the first spin-allowed LMCT transitions of $CrO_4^{2-}$ and $MnO_4^{2-}$ is thus 5500 cm$^{-1}$ rather than 8500 cm$^{-1}$. In addition, the Huang−Rhys parameter for the progression in the stretching mode in the first allowed LMCT band of $CrO_4^{2-}$ is about 3.6, and from eq 10 we obtain $\Delta r = 0.073$ Å. Apparently both quantities are substantially larger than those for $MnO_4^{2-}$. The decrease in the metal−oxygen bond strength upon LMCT excitation is thus larger for $CrO_4^{2-}$ than $MnO_4^{2-}$. Consequently, in $CrO_4^{2-}$ the set of e orbitals is stronger $\pi$ antibonding than in $MnO_4^{2-}$ and thus shifted to higher energy with respect to the set of $t_1$ ligand-centered orbitals.

## 5. Conclusions

Earlier assignments of the absorption spectrum of Mn-doped $BaSO_4$ suffered from the unrecognized coexistence of $MnO_4^{3-}$ and $MnO_4^{2-}$ in about the same ratio. By optimizing the preparation conditions, we were able to grow single crystals of manganese-doped $BaSO_4$ containing essentially $Mn^{6+}$. Their strongly polarized low-temperature absorption and luminescence spectra presented here allow an unambiguous band assignment in the approximate $C_{2v}$ point symmetry. It turns out that the striking differences between the spectra of Mn-doped $BaSO_4$ and $K_2SO_4$ reported earlier disappear if the simultaneous incorporation of $MnO_4^{2-}$ and $MnO_4^{3-}$ into $BaSO_4$ is prevented.

In transition-metal systems coupling of external lattice modes to the electronic transitions is usually very strong, leading to completely unstructured broad bands in the optical spectra. In the case of $MnO_4^{2-}$, however, the fine structure in the $^2E \leftrightarrow {}^2T_2$ LF spectra is well resolved, providing the key to a detailed analysis of the Jahn−Teller effects in the ground and excited states. It might thus be very interesting to stabilize $MnO_4^{2-}$ in a host lattice with a site of tetrahedral or trigonal symmetry. In

(27) Macfarlane, R. M.; Wong, J. Y.; Sturge, M. D. *Phys. Rev.* **1968**, *166*, 250.
(28) Hazenkamp, M. F.; Güdel, H. U. *J. Lumin.*, in press.
(29) Imbusch, G. F.; Kopelman, R. In *Laser Spectroscopy of Solids*; Yen, W. M., Selzer, P. M., Eds.; Springer-Verlag: Berlin, 1981; p 3.
(30) *Handbook of chemistry and physics*, 63rd ed.; CRC Press: Boca Raton, FL, 1982−1983.
(31) Cyvin, S. J. *Molecular Vibrations and Mean-Square Amplitudes*; Elsevier: Amsterdam, 1968.
(32) Ballhausen, C. J. *Theoret. Chim. Acta* **1963**, *1*, 285.
(33) Murthy, T. S. N.; Ramalingaiah, S.; Reddy, K. N.; Salagram, M. *Solid State Commun.* **1986**, *60*, 715.

these symmetries the $^2E$ ground state is unsplit, and we would expect a dynamic JT system. We are currently attempting to dope $MnO_4^{2-}$ into suitable host lattices.

From a practical point of view it is conceivable that the $BaSO_4$:$Mn^{6+}$ system has some potential as a tunable near-IR solid-state laser material because of its high radiative rate constant and moderate temperature quenching. The luminescence extends from 11 000 to about 6500 $cm^{-1}$; an extremely broad range in a very interesting region for possible laser applications. Radiative transition rates are considerably larger in tetrahedral than in octahedral systems because of lack of an inversion center in $T_d$ symmetry. This allows radiative processes to compete with nonradiative processes even at room temperature in the near-IR beyond 1 $\mu$m.

**Acknowledgment.** We thank Karl Krämer for his help with crystal growth and the Swiss National Science Foundation for financial support.

IC9611711